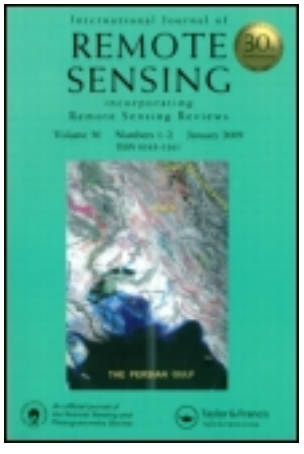

International Journal of Remote Sensing

Publication details, including instructions for authors and subscription information:
http://www.tandfonline.com/loi/tres20

Particle swarm optimization-based sub-pixel mapping for remote-sensing imagery

Qunming Wang [a], Liguo Wang [a] & Danfeng Liu [a]

[a] College of Information and Communications Engineering, Harbin Engineering University, Harbin, 150001, China

Version of record first published: 23 May 2012.

To cite this article: Qunming Wang, Liguo Wang & Danfeng Liu (2012): Particle swarm optimization-based sub-pixel mapping for remote-sensing imagery, International Journal of Remote Sensing, 33:20, 6480-6496

To link to this article: http://dx.doi.org/10.1080/01431161.2012.690541

International Journal of Remote Sensing
Vol. 33, No. 20, 20 October 2012, 6480–6496

Taylor & Francis
Taylor & Francis Group

Particle swarm optimization-based sub-pixel mapping for remote-sensing imagery

QUNMING WANG*, LIGUO WANG and DANFENG LIU
College of Information and Communications Engineering, Harbin Engineering University, Harbin 150001, China

(*Received 10 September 2010; in final form 1 September 2011*)

Mixed pixels are widely existent in remote-sensing imagery. Although the proportion occupied by each class in mixed pixels can be determined by spectral unmixing, the spatial distribution of classes remains unknown. Sub-pixel mapping (SPM) addresses this problem and a sub-pixel/pixel spatial attraction model (SPSAM) has been introduced to realize SPM. However, this algorithm fails to adequately consider the correlation between sub-pixels. Consequently, the SPM results created by SPSAM are noisy and the accuracy is limited. In this article, a method based on particle swarm optimization is proposed as post-processing on the SPM results obtained with SPSAM. It searches the most likely spatial distribution of classes in each coarse pixel to improve the SPSAM. Experimental results show that the proposed method can provide higher accuracy and reduce the noise in the results created by SPSAM. When compared with the available modified pixel-swapping algorithm, the proposed method often yields higher accuracy results.

1. Introduction

Remote-sensing techniques have been used in more and more application fields, such as agriculture, forestry, geology and oceanology. However, mixed pixels are widely existent in remote-sensing imagery, which has brought great difficulty in visual inspection and post-application. After all classes included are known, there are two main kinds of information that are of interest concerning mixed pixels. One is the proportion occupied by each class in mixed pixels. The other is the distribution of all classes within mixed pixels. Spectral unmixing (Keshava and Mustard 2002) and sub-pixel mapping (SPM) (Atkinson 1997) or super-resolution mapping techniques are put forward aimed at these two problems. By SPM, the distribution of land-cover classes can be mapped quantitatively, which can enhance the spatial resolution of images.

In recent years, SPM has become the hot issue in the remote-sensing domain, and some researchers have addressed the problem. Atkinson (1997) initially proposed the concept of SPM and the spatial dependence theory with the assumption that land cover is spatially dependent both within and between pixels; that is, compared with distant pixels, neighbouring pixels are more likely to be of the same land-cover class. Tatem *et al*. (2001a,b, 2002) and Nguyen *et al*. (2005) applied a method that used the

*Corresponding author. Email: wqm11111@126.com

International Journal of Remote Sensing
ISSN 0143-1161 print/ISSN 1366-5901 online © 2012 Taylor & Francis
http://www.tandfonline.com
http://dx.doi.org/10.1080/01431161.2012.690541

output from a fuzzy classification to constrain a Hopfield neural network based on the energy minimization principle. Atkinson (2001, 2005) introduced a pixel-swapping algorithm (PSA) that swapped two sub-pixels most in need of exchange within a coarse resolution pixel during each iteration. Verhoeye and De Wulf (2002) adopted linear optimization techniques to maximize spatial dependence. Mertens *et al*. (2003a), Wang *et al*. (2006) and Zhang *et al*. (2008) presented an approach based on a supervised back-propagation (BP) neural network. Teerasit *et al*. (2005) and Kassaye (2006) used a Markov random field to generate SPM results. Mertens *et al*. (2006) applied a sub-pixel/pixel spatial attraction model (SPSAM) that realized the spatial dependence theory directly.

Instead of iteratively optimizing spatial correlations among sub-pixels, SPSAM directly estimates the class of sub-pixels according to the proportion of its neighbouring pixels in a class. As such, the algorithm requires no iteration to achieve the spatial allocation of sub-pixel classes. The advantage of this algorithm is that it is suitable for real-time processing (Shen *et al*. 2009). Particularly, when dealing with situations involving a large scale factor, it is fast in obtaining the SPM results. However, the algorithm fails to consider adequately the correlation between sub-pixels. When the scale factor is large, there can be many isolated pixels and much noise. If we apply the algorithm to real remote-sensing imagery, where the spatial distribution of each class is diverse and changeable, there may be many sawtooth-shaped edges in the SPM results.

Owing to the drawbacks mentioned above, an approach based on particle swarm optimization (PSO) is put forward in this article and this searches the best solution for every mixed pixel after the SPSAM procedure to improve the SPSAM.

2. Methods

2.1 *Basic theory of SPM: spatial dependence theory*

For the convenience of understanding, here we provide a simple example to illustrate the spatial dependence theory (Verhoeye and De Wulf 2002). A simple representation of SPM is given in figure 1. It shows a raster grid of 3 × 3 coarse spatial resolution pixels with associated proportions of one land-cover class in figure 1(*a*), which can be obtained by spectral unmixing. A single coarse resolution pixel is divided into 2 × 2 sub-pixels, each corresponding to a 25% area of coarse low-resolution pixels. From the proportions, the number of sub-pixels belonging to this class can be calculated. For example, the fraction of 75% corresponds to three sub-pixels. One possible arrangement is shown in figure 1(*b*), where the black circles represent sub-pixels of the class.

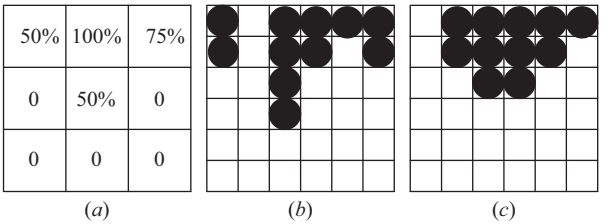

Figure 1. An easy explanation of spatial dependence theory. (*a*) The proportion image of one land-cover class, (*b*) one possible distribution of the class and (*c*) another possible distribution of the class.

Obviously, its spatial structure conflicts with expectations of spatial dependence. This is because, in nature, the land cover coming from the same classes is more likely to stay together. Another solution is presented in figure 1(*c*). It can be seen that, compared with figure 1(*b*), the spatial dependence both within and between the coarse pixels in figure 1(*c*) is much stronger. Therefore, figure 1(*c*) is a more reasonable SPM result.

2.2 *Mathematic model of spatial dependence: SPSAM*

Mertens *et al*. (2006) applied SPSAM and realized the spatial dependence theory in a simple and effective way. In SPSAM, attractions between each sub-pixel within a coarse resolution pixel and its neighbour pixels are calculated in order to determine the spatial distribution of sub-pixels per class. Assume p_{ij} is a sub-pixel in pixel P_{ab} and P_k is one of P_{ab}'s neighbours. Then the attraction from class c for sub-pixel p_{ij} is calculated as

$$\text{Attraction}_{c,p_{ij}} = \sum_{k=1}^{n} \lambda_k F_c(P_k), \tag{1}$$

where n is the total number of neighbours (in this article, n is set to 8) and $F_c(P_k)$ is the fraction value of the kth neighbouring pixel P_k for class c. λ_k is the measurement of spatial dependence and is calculated as

$$\lambda_k = [d(p_{ij}, P_k)]^{-1}, \tag{2}$$

where $d(p_{ij}, P_k)$ is the Euclidean distance between geometric centres of sub-pixel p_{ij} and its neighbouring pixel P_k and is calculated as

$$d(p_{ij}, P_k) = \sqrt{(x_{ij} - X_k)^2 + (y_{ij} - Y_k)^2}. \tag{3}$$

Finally, $\text{Attraction}_{c,p_{ij}}$ for each class can be used for the assignment of sub-pixels to the different classes: sub-pixels with highest attractions are assigned first. The SPSAM algorithm is much easier for the situation of two land-cover classes. Suppose there are two classes A and B. We can conduct the SPSAM as follows: within a coarse resolution pixel P_{ab}, each p_{ij}'s $\text{Attraction}_{c,p_{ij}}$ is first calculated by equations (1)–(3) and then the values are ranked in order. Finally, the $F_A(P_{ab})\, S^2$ ($F_A(P_{ab})$ is the fraction value of class A within pixel P_{ab} and S is a scale factor) sub-pixels with high values of $\text{Attraction}_{c,p_{ij}}$ are assigned to class A while the residual ones are assigned to class B (Mertens *et al*. 2004). This approach can also be extended to multiple classes.

2.3 *Methods that can be used as post-processing on SPSAM*

From §2.2, we can see that the SPSAM algorithm directly estimates the class of sub-pixels according to the class proportion of its neighbouring pixels. However, the algorithm fails to adequately consider the correlation between sub-pixels, and thus it may lead to poor performance for SPM. Shen *et al*. (2009) adopted a method that created a modified pixel-swapping algorithm (MPS) with initialization from SPSAM. Although its original purpose was to improve the PSA, it can be regarded as a method that enhances the performance of SPSAM as well by fully considering the correlation

between sub-pixels after SPSAM. In this section, the principle of PSA is described first, and then an objective function is proposed based on this principle. The objective function will be used for the searching process by PSO in the next section and will also be used as a post-processing method after the SPSAM procedure.

2.3.1 Pixel-swapping algorithm. Atkinson (2001, 2005) proposed the PSA. The objective was to vary the spatial arrangement of the sub-pixels in such a way that the spatial correlation between neighbouring sub-pixels (both within and, perhaps more importantly, between pixels) would be maximized. Two classes are taken into account: '1' and '0'. For each sub-pixel p_{ij}, the attraction caused by all its neighbouring sub-pixels is calculated as

$$O_{p_{ij}} = \sum_{k=1}^{n} \lambda_k z(p_k), \tag{4}$$

where n is the total number of neighbours, $z(p_k)$ is the binary value of the class for p_k and λ_k is the measurement of spatial correlation between sub-pixels and is calculated as

$$\lambda_k = \exp\left(\frac{-d_k}{a}\right), \tag{5}$$

where a is a non-linear parameter of the exponential model and d_k is the Euclidean distance between geometric centres of sub-pixel p_{ij} and its neighbouring sub-pixel p_k, as in equation (3). We can see that $O_{p_{ij}}$ indicates the attraction for p_{ij} caused by class '1' from its neighbouring sub-pixels.

After each p_{ij}'s $O_{p_{ij}}$ has been calculated, the following two-stage process is conducted for each pixel P_{ab}:

Stage 1: Rank all $O_{p_{ij}}$ in decreasing order. As a result, a corresponding sequence (sequence$_a$) is generated, which is composed of the binary values of the class for p_{ij}.

Stage 2: Identify the first '0' from left and the first '1' from right in the sequence. If the '0' locates before the '1', then the two values are swapped to increase the total attraction inside P_{ab}. Otherwise, no change is made.

The above two-stage process is repeated iteratively. The process can be stopped either at a fixed number of iterations or when little change is made. PSA was first used to work for two classes. Afterwards, Thornton *et al*. (2006), Makido (2006) and Makido *et al*. (2007) extended the algorithm to deal with multiple classes.

Figure 2 exhibits the whole iteration process of PSA for a single pixel when the scale factor $S = 3$. As shown in figure 2, the goal of the algorithm is to modify the sequence$_a$, so that all 1's are located before all 0's in the new sequence. In this situation, the total attraction for class '1' sub-pixels caused by '1' from their neighbouring sub-pixels is maximized and the same holds for class '0'. Consequently, inside P_{ab}, the sum of the attraction for each sub-pixel caused by sub-pixels from the same class is also maximized. In fact, the real iteration process is not so simple and smooth, and sometimes the required sequence cannot be obtained, owing to the influence or attraction from p_{kn}. p_{kn} indicates those sub-pixels that are within P_{ab}'s neighbouring pixels

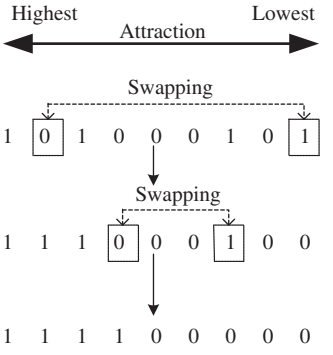

Figure 2. The whole iteration process of PSA for a single pixel.

as well as the neighbours of p_{ij}. That is because PSA has a great likelihood of falling into local minima (Atkinson 2001), which can be explained from the point of view of the evolution algorithm. The algorithm swaps only two sub-pixels each time and the 'evolution pace' is so slow that it may give rise to premature convergence and fall into local minima. Therefore, we can conclude that the accuracy of SPM results generated by MPS is limited.

2.3.2 An objective function. Having studied the feature of sequence$_a$, we can construct an objective function that makes the correlation between sub-pixels reach maximum after the SPSAM process. Again the two classes are regarded: '1' and '0', i.e. p_{ij} takes 1 or 0 for an unmixed pixel P_{ab}. The objective function with the constraint condition can be written as

$$\begin{aligned} \max\ J &= \sum_{i=1}^{S}\sum_{j=1}^{S}\left[p_{ij}\boldsymbol{\alpha}\mathbf{N}_{p_{ij}} + (1-p_{ij})\,\boldsymbol{\alpha}\left(\boldsymbol{I}^{\mathrm{T}} - \boldsymbol{N}_{p_{ij}}\right)\right] \\ \text{s.t.}\quad &\sum_{i=1}^{S}\sum_{j=1}^{S} p_{ij} = F(P_{ab})\,S^2, \end{aligned} \tag{6}$$

where $F(P_{ab})$ is the proportion of class '1' in P_{ab} and $\boldsymbol{N}_{p_{ij}}$ is a vector composed of the class values of p_{ij}'s neighbouring sub-pixels: $\boldsymbol{N}_{p_{ij}} = \left[p_{i-1,j-1}, p_{i-1,j}, p_{i-1,j+1}, p_{i,j-1}, p_{i,j+1}, p_{i+1,j-1}, p_{i+1,j}, p_{i+1,j+1}\right]^{\mathrm{T}}$. It should be noticed that when $i = 1$ or $j = 1$, the subscript of some of $\boldsymbol{N}_{p_{ij}}$'s elements is equal to 0, which indicates the sub-pixels p_{kn} in §2.3.1. $\boldsymbol{\alpha}$ is a vector used as the measurement of spatial correlation between sub-pixels: $\boldsymbol{\alpha} = \left[\exp\left(-\frac{d_1}{a}\right), \exp\left(-\frac{d_2}{a}\right), \ldots, \exp\left(-\frac{d_8}{a}\right)\right]$, where d_k ($k = 1, 2, \ldots, 8$) is the distance between p_{ij} and the kth neighbouring sub-pixel. $\boldsymbol{I}^{\mathrm{T}}$ is a vector composed of elements of 1's.

If p_{ij} belongs to class '1' ($p_{ij} = 1$), the attraction for the sub-pixel caused by '*1*' from its neighbours can be calculated by the first term of equation (6). In contrast, if p_{ij} belongs to class '0' ($p_{ij} = 0$), the attraction for the sub-pixel caused by '0' from its neighbours can be calculated by the second term of equation (6). As a result, inside

P_{ab}, the total attraction for all of the sub-pixels caused by the same class can be calculated by equation (6). When the correlation between sub-pixels is maximized, J reaches maximum. Hence, by solving equation (6), we can get the most suitable distribution of all sub-pixels within the mixed pixel by evaluating all possible configurations and selecting the one that makes J reach maximum. However, it mainly works well for small images with a small scale factor (Mertens *et al*. 2003b). With a large scale factor, the number of combinations of possible spatial distribution increases dramatically and the computational load may become unrealistic. For this reason, there is a need to introduce an effective optimization algorithm to handle the problem. In this article, a PSO technique is presented and it is discussed in detail in the next section.

2.4 *PSO-based SPM*

2.4.1 Introduction to PSO. The PSO, originally developed by Kennedy and Eberhart (1995), was inspired by the social behaviour of bird flocking or fish schooling for food. It is an evolutionary computation technique based on swarm intelligence. In comparison with other evolution algorithms, PSO reserves the global searching strategy based on community and yet avoids complex genetic operators with a simple speed-offset model that requires fewer parameters. It traces the current searching situation and tunes the strategy when necessary for strong memory, which makes PSO easy to realize. PSO has powerful global convergence with a stronger robustness optimization algorithm (Kennedy *et al*. 2001) that has been widely used in neural network training (Li *et al*. 2010), non-linear programming (Zhi *et al*. 2004), multi-objective optimization and many other areas (Akjiratikarl *et al*. 2007, Liu *et al*. 2008).

The initial PSO is operated in the continuous-valued space, where coordinates for every particle's position and velocity are coded as real numbers in each dimension. In 1997, Kennedy and Eberhart proposed a reworking of the algorithm to operate on discrete binary variables. In the binary PSO, coordinates for position will take on a 1 or 0 value, but it is not for velocity. The mathematical description of the binary PSO is as follows. Each particle i consists of two vectors, position and velocity, which can be represented by $\boldsymbol{X}_i = [X_{i1}, X_{i2}, \ldots, X_{im}]$ and $\boldsymbol{V}_i = [V_{i1}, V_{i2}, \ldots, V_{im}]$, respectively, where m is the dimension of the search space. One position vector $\boldsymbol{X}_i$ corresponds to one solution to the optimization problem. The position and velocity are updated as

$$\begin{aligned} V_{ip}(t) = {} & wV_{ip}(t-1) + c_1\mathrm{rand}_1[P_{ip}(t-1) \\ & - X_{ip}(t-1)] + c_2\mathrm{rand}_2[G_p(t-1) - X_{ip}(t-1)], \end{aligned} \tag{7}$$

$$\mathrm{sig}[V_{ip}(t)] = \frac{1}{1+\exp[-V_{ip}(t)]}, \tag{8}$$

$$X_{ip}(t) = \begin{cases} 1, & \mathrm{rand} < \mathrm{sig}[V_{ip}(t)] \\ 0, & \mathrm{rand} \geq \mathrm{sig}[V_{ip}(t)] \end{cases}, \tag{9}$$

where $i = 1, 2, \ldots, M$, with i representing the ith particle and M the size of the swarm; t is the number of generations; sig means sigmoid function; $V_{ip}(t)$ and $X_{ip}(t)$ mean the coordinate values of the pth dimension of velocity $\boldsymbol{V}_i$ and the pth dimension of spatial position $\boldsymbol{X}_i$ at the tth generation; $P_{ip}(t-1)$ is the coordinate value of the

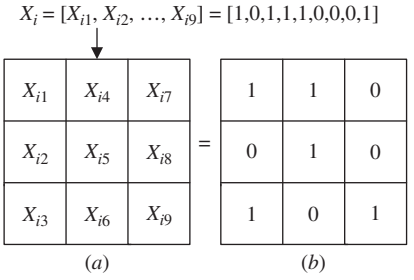

Figure 3. (*a*) The position of the *i*th particle and (*b*) its corresponding solution ($S = 3$).

*p*th dimension of $\boldsymbol{P}_i(t-1)$ that indicates the best solution for particle i from the first to the $(t-1)$th generation; $G_p(t-1)$ is the coordinate value of the *p*th dimension of $\mathbf{G}(t-1)$ that indicates the best position or solution in the whole swarm during the $(t-1)$th generation; w is the inertia weight coefficient; c_1 and c_2 are learning rates, that is they are non-negative constants and usually both are set to 2; and rand_1 and rand_2 are independent random numbers between 0 and 1.

2.4.2 PSO after SPSAM process. At first, the correspondence between the position of a random particle and its solution is illustrated in figure 3, where the scale factor $S = 3$. The solution in figure 3(*b*) is the spatial distribution of classes '1' and '0' in a mixed pixel.

Then, suppose the SPM result SuperA is acquired by the SPSAM procedure and PSO is implemented after it, with the whole process executed as follows.

Stage 1. A mixed pixel P_{ab} in a coarse low-resolution image (i.e. fraction image) is selected in order and the following six steps of processing are carried out.

Step 1. A swarm with M particles is formed with the dimension number S^2 for each particle i, $i = 1, 2, \ldots, M$. Necessarily, the total number (defined as N_i) of sub-pixels that belong to class 1 must be $F(P_{ab})S^2$. For a mixed pixel P_{ab}, a certain particle can be extracted from SuperA, the position of which corresponds to the spatial distribution of the classes in P_{ab} itself. After that, the particular particle is cloned several times. Assume $\rho_{\text{clone}} \in (0,1)$ is the defined ratio. As a result, there will be $\rho_{\text{clone}} M$ clones generated in the swarm. ρ_{clone} cannot be too high, otherwise it will result in premature convergence and will fall into local optima.

Step 2. The initialization of the velocity for every particle: $\boldsymbol{V}_i = [V_{i1}, V_{i2}, \ldots, V_{im}]$, $i = 1, 2, \ldots, M$, where the *p*th dimension of the *i*th particle is initialized as

$$V_{ip} = V_{\min} + \text{rand}(V_{\max} - V_{\min}),\ p = 1, 2, \ldots, S^2. \tag{10}$$

We can set $V_{\min} = -V_{\max}$ and then V_{ip} is restricted to the interval $[-V_{\max}, V_{\max}]$.

Step 3. According to equation (6), the fitness J_{Xi} of each particle is calculated. Afterwards, the particle $\boldsymbol{G}(t)$ that has the highest fitness is selected and it is just the best position in the whole swarm at the *t*th generation. Besides, the best position $\boldsymbol{P_i}(t)$ for particle i from the first to the *t*th generation is also selected in the same way. By using

equations (7)–(9), the position and velocity are updated, after which the velocity is restricted as

$$V_{ip}(t) = \begin{cases} V_{\max}, & V_{ip}(t) > V_{\max} \\ V_{ip}(t), & -V_{\max} \le V_{ip}(t) \le V_{\max} \\ -V_{\max}, & V_{ip}(t) < -V_{\max} \end{cases}, \tag{11}$$

which can prevent the particles from falling into local optima and flying over the best position.

Step 4. The constraint in equation (6) is realized. After one update, N_i may not be $F(\mathrm{P}_{ab})S^2$ and measures should be taken to maintain the constraint, which can be realized as follows: if N_i is bigger than $F(\mathrm{P}_{ab})S^2$, $N_1 - F(\mathrm{P}_{ab})S^2$ particles that belong to class '1' are randomly selected and changed into '0' while, on the contrary, the selected ones are change into '1'.

Step 5. Swarm goes through R times evolution according to steps 3 and 4.

Step 6. The best position X_{best} during all generations is found out and used to re-decide the spatial distribution of the classes within P_{ab} in SuperA.

Stage 2. For all mixed pixels in the fraction image, stage 1 is processed.

Stage 3. The behaviour of the swarm is affected by sub-pixels that are part of neighbouring coarse resolution pixels (i.e. p_{kn}) and changes in one coarse resolution pixel should have an influence on neighbouring coarse resolution pixels. Therefore, stages 1 and 2 are repeated Q times, and the SPM result SuperB based on PSO is approached iteratively.

Figure 4 displays the whole PSO-based SPM process, where r and h denote the counters of generations and iterations, respectively.

When the total number of classes is C, then we can construct C one-against-rest models. In each model, one class is selected as class '1' and other classes are treated as class '0'. Then the spatial distribution of class '1' is determined. At last, C sub-pixel maps will be generated. Theoretically, the boundaries of each class within the coarse resolution pixel may compete with each other. An effective way to integrate the C sub-pixel maps and get the SPM results for multiple classes is to choose the boundary of each class as a common boundary in turn (Ge *et al*. 2009). For each coarse resolution pixel, once the first class is allocated in agreement with its boundary, only the remaining sub-pixels are used to allocate the second class in agreement with the boundary of this class. This ordered allocation procedure continues until the final class is allocated. In this way, the order of these classes must be specified at first. Makido *et al*. (2007) have advocated a method using Moran's I to determine the order. However, this method requires prior class information, which is not obtainable in most real situations. To avoid complex procedures, here a simple and effective method is applied. Instead of starting to allocate sub-pixels of the dominant class surrounded by many neighbours, it may seem reasonable to first determine the distribution of the rare sub-pixels among them (Mertens *et al*. 2006). For this reason, for each selected coarse resolution pixel, the classes within it can be ranked according to their fractions from this pixel's neighbours and the class with smaller fraction is allocated before the classes with larger fractions.

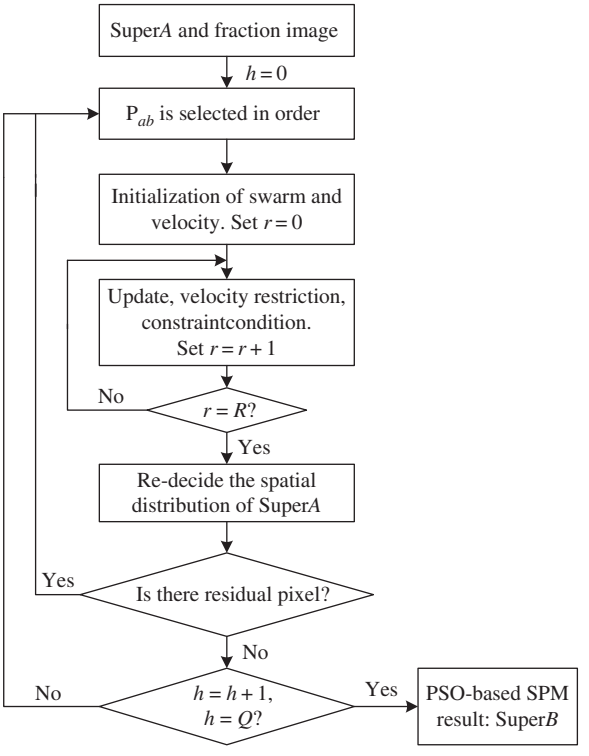

Figure 4. Flowchart of PSO-based SPM after SAM.

3. Experiments and results

The SPM is usually a post-process on spectral unmixing and should be processed on fraction images. If this approach is used, errors due to co-registration and poor unmixing will be introduced. To concentrate solely on the performance of the proposed SPM algorithm, in these experiments, the algorithm is tested on only synthetic fraction images. These images can be created by degrading real or artificial high spatial resolution images via a mean filter (Yi *et al*. 2006). In this way, the resulting fraction images contain little uncertainty since they originate from degradation (Ge *et al*. 2009). Last but not least, the SPM outcomes can be assessed by comparing with the truth reference images; hence, the assessment will be reliable.

At first, in this section, we provide the results of three experiments based on four methods: traditional hard classification (HC), SPSAM, MPS and PSO. Then, the influences of PSO parameters are discussed in the last experiment. In the first two experiments, the accuracy is calculated in terms of the root mean square error (RMSE) and a new coefficient H. RMSE can be written as

$$\mathrm{RMSE} = \sqrt{\frac{\sum_{q=1}^{n} (y_q - x_q)^2}{n}}, \tag{12}$$

where n is the total number of pixels in high spatial resolution images, y is a set of grey values in the real image and x is a set of grey values in the prediction image. It can

be inferred that RMSE is quite suitable for the assessment of two land-cover classes. In fact, when only two classes exist, the best way to evaluate the difference between the real and prediction images is to subtract one from another and measure the difference value, as in the numerator of equation (12). A new coefficient H is applied and it is calculated as

$$H = \left(\frac{\mathrm{RMSE_a}}{\mathrm{RMSE_h}}\right)^2, \tag{13}$$

where $\mathrm{RMSE_h}$ represents RMSE for HC and $\mathrm{RMSE_a}$ represents RMSE for a certain SPM algorithm. The advantage of this coefficient is that $\mathrm{RMSE_h}$ builds the bridges for the assessment of each SPM algorithm, which means that the outcome of each algorithm can be compared not only with that of HC but also mutually by evaluating H. It can take out the effect brought by a number of pure pixels in coarse spatial resolution images by removing n in equation (13). It is easy to conclude that the lower the values of RMSE and H, the better the performance.

However, when the number of classes is more than two, the subtraction in RMSE cannot be simply conducted and H is obviously not appropriate either. For this reason, in the third experiment, which is conducted on a real remote-sensing image including multiple classes, the accuracy is evaluated by calculating classical kappa coefficient (Cohen 1960) and the overall accuracy is evaluated in terms of the percentage of correctly classified pixels (PCC). In addition, another two indexes Kappa' and PCC' are also used, which are calculated only for mixed pixels and thus can eliminate the influence of pure pixels, just as H above. These pure pixels have plentiful sub-pixels, which all belong to the same class and will only raise the kappa coefficient and PCC without providing information on the algorithm's prediction abilities (Mertens *et al*. 2003b).

3.1 *Experiment 1: artificial images*

In the first experiment, three artificial images are tested: circle, cross-line and words. Tables 1 and 2 show the accuracy measurement of each method with scales 2 and 4, respectively. Values in bold indicate the lowest RMSE or H. All SPM results have lower RMSE and H values than HC, which leads to the conclusion that SPM makes sense. When the scale factor is 2, there is little difference between the performances of three SPM algorithms. MPS has the highest accuracy because it is less likely for MPS to fall into local minima with a small scale factor. Furthermore, table 1 demonstrates that SPSAM has low RMSE and H with a low scale. With a higher scale, the number

Table 1. Accuracy measurement of each method with scale 2 for artificial images.

	RMSE				*H*			
	HC	SPSAM	MPS	PSO	HC	SPSAM	MPS	PSO
Circle	0.0975	**0**	**0**	**0**	1	**0**	**0**	**0**
Cross-line	0.1136	**0**	**0**	**0**	1	**0**	**0**	**0**
Words	0.1554	0.0226	**0.0202**	0.0226	1	0.0214	**0.0171**	0.0214

Note: Values in bold indicate the lowest RMSE and *H*.

Table 2. Accuracy measurement of each method with scale 4 for artificial images.

	RMSE				*H*			
	HC	SPSAM	MPS	PSO	HC	SPSAM	MPS	PSO
Circle	0.1418	0.0447	**0.0283**	0.0346	1	0.0995	**0.0398**	0.0597
Cross-line	0.1741	0.0510	0.0490	**0.0316**	1	0.0858	0.0792	**0.0330**
Words	0.2219	0.1258	0.1102	**0.1020**	1	0.3212	0.2466	**0.2114**

Note: Values in bold indicate the lowest RMSE and *H*.

of sub-pixels increases and the SPM problem becomes more complex. When the scale factor is 4, RMSE and *H* values from SPSAM are the highest for all three images except the HC method, which illustrates that SPSAM is not very reliable with a high scale. For cross-line and words images, PSO has the best effect. However, for the circle image, the effect of MPS is superior to PSO, which can be explained by the fact that the circle has the most compact two-dimensional shape and it is the easiest for the algorithm (Atkinson 2001).

Visual assessment, however, remains very important. The three truth images and the corresponding results obtained by each method with scale 4 for all three images are illustrated in figure 5. The information of the boundary in images is almost lost in figure 5(*b*) when HC is applied. In the results of SPSAM (figure 5(*c*)), there are many pits and isolated pixels, especially in the words image. Meanwhile, SPSAM fails to restore the right-angle shape. MPS has enhanced the performance of SPSAM to a certain degree, but the performance in figure 5(*d*) is less satisfying in comparison with PSO. It can be seen in figure 5(*e*) that PSO has restored most of the shapes such as right-angle shape and there are nearly no pits and isolated pixels, which is more reasonable and close to the original reference images.

3.2 *Experiment 2: binary fraction images of HSI*

Binary fraction images of hyperspectral imagery (HSI) are used in this experiment. The HSI data were acquired in the Indian Pine Test Site in June 1992. It covers an

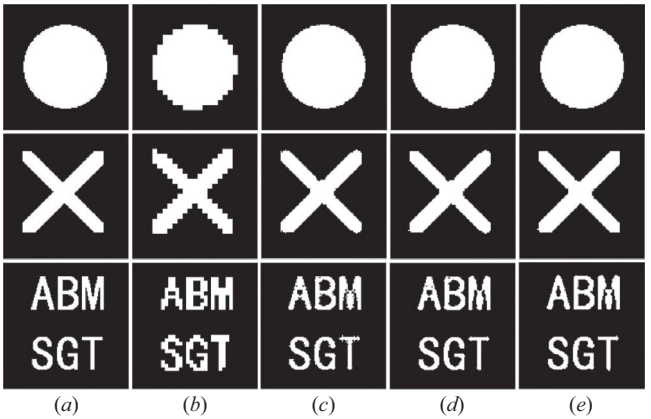

Figure 5. Experimental results of artificial images with scale 4. Line 1: circle; line 2: cross-line; line 3: words. (*a*) Original reference images, (*b*) HC results, (*c*) SPSAM results, (*d*) MPS results and (*e*) PSO results.

Table 3. Accuracy measurement of each method with scale 2 for binary fraction images of HSI.

	RMSE				*H*			
	HC	SPSAM	MPS	PSO	HC	SPSAM	MPS	PSO
Class 12	0.1146	0.0177	**0**	**0**	1	0.0238	**0**	**0**
Class 14	0.0873	0	**0**	**0**	1	0	**0**	**0**

Note: Values in bold indicate the lowest RMSE and *H*.

Table 4. Accuracy measurement of each method with scale 4 for binary fraction images of HSI.

	RMSE				*H*			
	HC	SPSAM	MPS	PSO	HC	SPSAM	MPS	PSO
Class 12	0.1668	0.0829	0.0707	**0.0661**	1	0.2472	0.1798	**0.1573**
Class 14	0.0962	0.0417	0.0295	**0.0278**	1	0.1875	0.0938	**0.0833**

Note: Values in bold indicate the lowest RMSE and *H*.

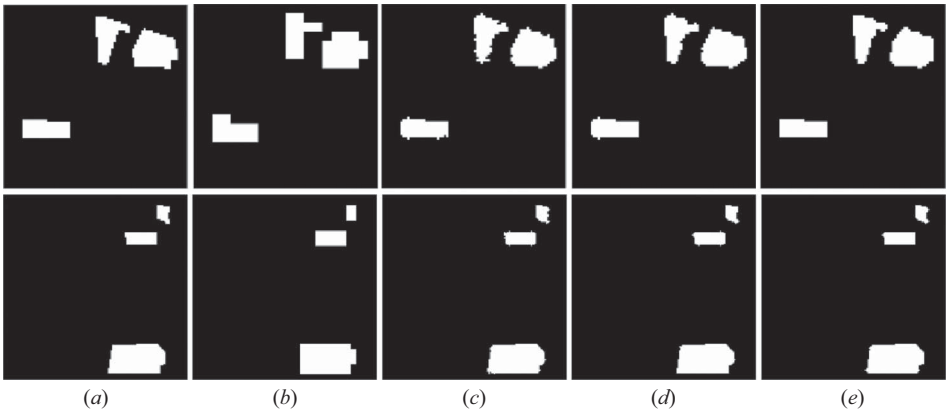

Figure 6. Experimental results of binary fraction images of HSI with scale 4. Line 1: class 12; line 2: class 14. (*a*) Original reference images, (*b*) HC results, (*c*) SPSAM results, (*d*) MPS results and (*e*) PSO results.

agriculture/forestry landscape and has 16 classes. The land-cover map of classes 12 (soybeans-clean) and 14 (woods) are selected for testing. The accuracy measurements of each method with scales 2 and 4 are shown in tables 3 and 4, respectively. Figure 6 presents the reference images and some corresponding results by each method with a scale of 4.

Similar to previous tests, the performance of HC is the worst among these methods, and lower error outcome can be achieved by SPSAM only when the scale factor is lower, as shown in table 3. As for higher scales, MPS and PSO are implemented after SPSAM process. They can provide higher accuracy SPM results. Among these methods, PSO has the lowest RMSE and *H* values and the most accurate SPM results in this experiment.

3.3 *Experiment 3: real remote-sensing image*

In this experiment, the methods are tested on a real remote-sensing image of 280 × 280 pixels (at 30 m spatial resolution) covering Taihu Lake located at the junction of Jiangsu and Zhejiang provinces, China. The image was acquired by the HJ-1 satellite launched in 2008 in China. An iterative self-organizing data (ISODATA) analysis technique is applied to this image and a land-cover map is generated containing three land classes: water, vegetation and soil. A colour version of this image is available at the website http://www.cresda.com/n16/n1190/index.html.

The image results with scale 4 are given in figure 7, and the accuracy assessment for each method is shown as a bar chart in figure 8. As can be seen from figure 8, when Kappa' and PCC' are compared, the differences of the four methods are more distinct. When applied to multiple classes, the performance of PSO is a little poorer than that of MPS and both of them are superior to SPSAM and HC in performance.

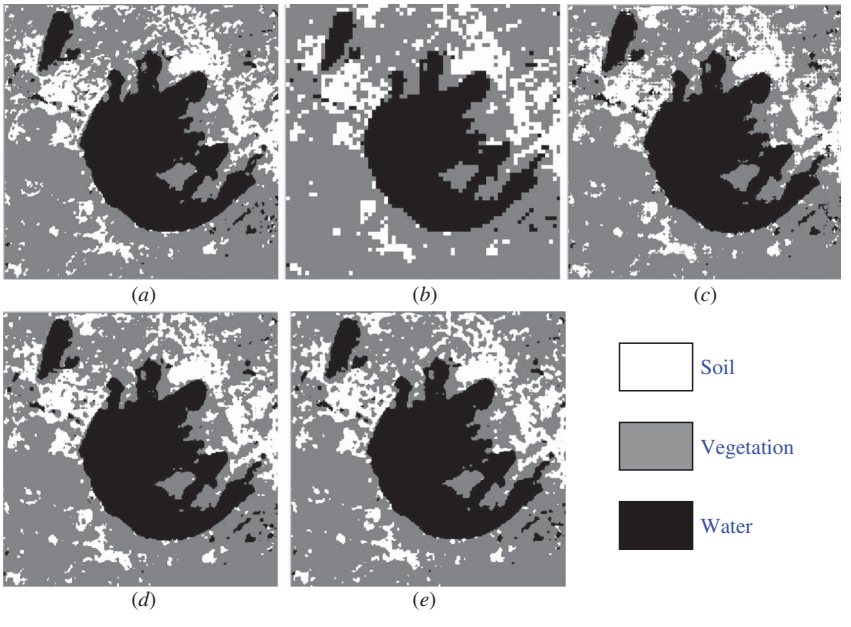

Figure 7. Experimental results of a real remote-sensing image with scale 4. (*a*) Original reference image, (*b*) HC result, (*c*) SPSAM result, (*d*) MPS result and (*e*) PSO result.

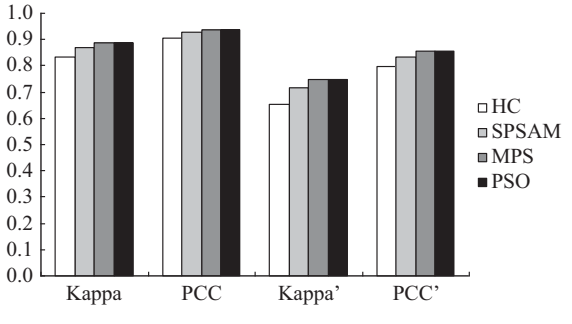

Figure 8. Four coefficients of different methods for a real remote-sensing image.

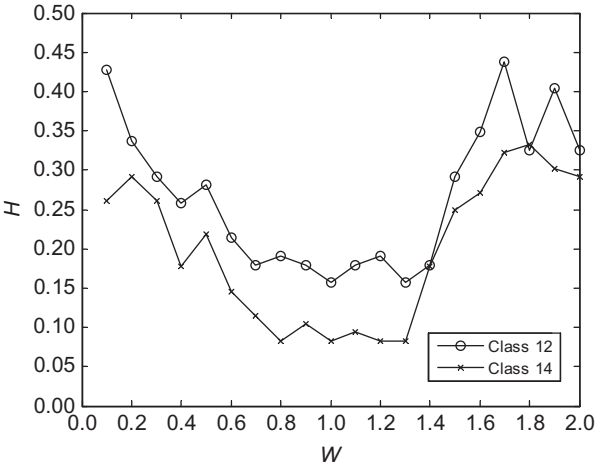

Figure 9. H of the proposed PSO-based SPM results for classes 12 and 14 with variable w ($c_1 = c_2 = 2$).

As shown in figure 7(*a*), the spatial arrangement of three land-cover classes does not completely meet the assumption of spatial dependence. Consequently, the differences between PSO and MPS are acceptable and can even be ignored. We can hold the view that PSO and MPS have nearly the same performance on SPM for the remote-sensing image used in this experiment. From figure 7, it can be observed that a considerable amount of detail is lost in the HC result while many sawtooth edges appear in SPSAM. As for MPS and PSO, most of the detail is restored and the results are more acceptable and close to the original reference image.

3.4 *Experiment 4: influences of parameters of PSO*

w, c_1 and c_2 are three important parameters of PSO. In order to analyse their influences on SPM results, two images in experiment 2 (classes 12 and 14) are used for the test with scale 4. As to w, we study the performance of the proposed PSO-based SPM when w ranges from 0.1 to 2 with step size 0.1, and c_1 and c_2 are both set to 2. It can be learned from the curves in figure 9 that the effect of the proposed method is considerably sensitive to the variation of w. When w takes values in the range [0.8, 1.3], it is more likely to produce satisfying SPM results.

Next, w is set to 1 and the influences of c_1 and c_2 are studied. It should be noticed that c_2 is set to 2 when c_1 varies while c_1 is set to 2 when c_2 varies. The two parameters range from 0.5 to 5 with step size 0.5. As illustrated in figure 10, H of the PSO-based SPM results varies little when the two parameters increase. In other words, the proposed method is not sensitive to the variation of c_1 and c_2. In addition, in comparison with other values, more satisfying SPM results can be generated when $c_1 = c_2 = 2$.

4. Discussion and conclusions

An SPM method based on PSO is proposed after the SPSAM procedure in this article. It searches the most likely spatial distribution of classes within every coarse spatial resolution image pixel in order to overcome the drawback of SPSAM, which fails to consider the correlation between sub-pixels adequately. Experimental results show

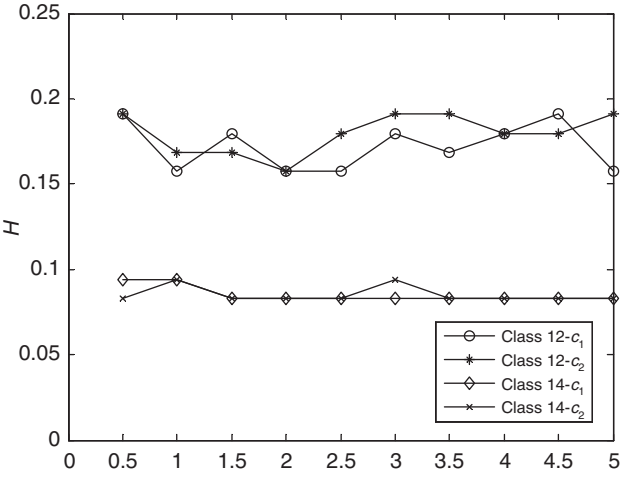

Figure 10. H of the proposed PSO-based SPM results for classes 12 and 14 with variables c_1 and c_2 ($w = 1$).

that the proposed method has enhanced the SPM effect of SPSAM and, compared with MPS, it often leads to higher accuracy SPM results.

It should be pointed out that PSO is not a unique optimization algorithm to search the optimal solution. The classical genetic algorithm (GA) and simulated annealing (SA) can also be taken into account. For example, when GA is applied, crossover and mutation are not allowed because these operators will disrupt the different fractions in the pixel. High-frequency exchange operators for each individual that is just like the particle in this article can be adopted. The major reason for applying PSO is because it has fast and powerful global convergence and strong robustness, and crucially, it is easy to realize with fewer parameters.

Although PSO-based SPM has provided higher accuracy results than SPSAM, with additional information, such as geometric shape, the altitude (Nguyen *et al*. 2005, Ling *et al*. 2008) and many other available features of each land-cover class, further improvement can be achieved without doubt. The additional information is of great importance to the SPM process of the diversely distributed real remote-sensing images. The proposed method can be further researched by improving PSO theory itself and constructing more appropriate object function. Further work will focus on these problems and further details will be acquired to complete the process of PSO-based SPM after SPSAM.

Acknowledgements

This work was supported by the National Natural Science Foundation of China under Grant No. 60802059 and Foundation for the Doctoral Programme of Higher Education of China under Grant No. 200802171003. The authors thank the reviewers for providing constructive comments.

References

Akjiratikarl, C., Yenradee, P. and Drake, P.R., 2007, PSO-based algorithm for home care worker scheduling in the UK. *Computers & Industrial Engineering*, **53**, pp. 559–583.

Atkinson, P.M., 1997, *Innovations in GIS 4*, pp. 166–180 (London: Taylor & Francis).

Atkinson, P.M., 2001, Super-resolution target mapping from soft-classified remotely sensed imagery. In *Proceedings of the 5th International Conference on GeoComputation*, University of Leeds, Leeds, UK.

Atkinson, P.M., 2005, Sub-pixel target mapping from soft-classified, remotely sensed imagery. *Photogrammetric Engineering & Remote Sensing*, **71**, pp. 839–846.

Cohen, J., 1960, A coefficient of agreement for nominal scales. *Educational and Psychological Measurement*, **20**, pp. 37–46.

Ge, Y., Li, S. and Lakhan, V.C., 2009, Development and testing of a subpixel mapping algorithm. *IEEE Transactions on Geoscience and Remote Sensing*, **47**, pp. 2155–2164.

Kassaye, R.H., 2006, Suitability of Markov random field-based method for super-resolution land-cover mapping. Master dissertation, International Institute for Geo-information Science and Earth Observation.

Kennedy, J. and Eberhart, R.C., 1995, Particle swarm optimization. In *Proceedings of the IEEE International Conference on Neural Networks*, Piscataway, NJ, pp. 1942–1948.

Kennedy, J. and Eberhart, R.C., 1997, A discrete binary version of the particle swarm algorithm. In *Proceedings of the World Multiconference on Systemics, Cybernetics and Informatics*, Piscataway, NJ, pp. 4104–4109.

Kennedy, J., Eberhart, R.C. and Shi, Y., 2001, *Swarm Intelligence* (San Francisco, CA: Morgan Kaufman Publishers).

Keshava, N. and Mustard, J.F., 2002, Spectral unmixing. *IEEE Signal Processing Magazine*, **19**, pp. 44–57.

Li, M., Wei, L. and Yang, C., 2010, A global convergence PSO training algorithm of neural networks. In *8th World Congress on Intelligence Control and Automation*, pp. 3261–3265.

Ling, F., Xiao, F., Du, Y., Xue, H.P. and Ren, X.Y., 2008, Waterline mapping at the sub-pixel scale from remote sensing imagery with high-resolution digital elevation models. *International Journal of Remote Sensing*, **29**, pp. 1809–1815.

Liu, X.P., Li, X., Peng, X.J., Li, H.B. and He, J.Q., 2008, Swarm intelligence for classification of remote sensing data. *Science in China Series D: Earth Sciences*, **51**, pp. 79–87.

Makido, Y., 2006, Land cover mapping at sub-pixel scales. PhD dissertation, Michigan State University, East Lansing, MI.

Makido, Y., Shortridge, A. and Messina, J.P., 2007, Assessing alternatives for modeling the spatial distribution of multiple land-cover classes at sub-pixel scales. *Photogrammetric Engineering & Remote Sensing*, **73**, pp. 935–943.

Mertens, K.C., Basets, B.D., Verbeke, L.P.C. and De Wulf, R.R., 2004, Direct sub-pixel mapping exploiting spatial dependence. *Proceedings of the International Geoscience and Remote Sensing Symposium*, **5**, pp. 3200–3202.

Mertens, K.C., Basets, B.D., Verbeke, L.P.C. and De Wulf, R.R., 2006, A sub-pixel mapping algorithm based on sub-pixel/pixel spatial attraction models. *International Journal of Remote Sensing*, **27**, pp. 3293–3310.

Mertens, K.C., Verbeke, L.P.C. and De Wulf, R.R., 2003a, Sub-pixel mapping with neural networks: real-world spatial configurations learned from artificial shapes. In *Proceedings of the 4th International Symposium on Remote Sensing of Urban Areas*, Regensburg, Germany, pp. 117–121.

Mertens, K.C., Verbeke, L.P.C., Ducheyne, E.I. and De Wulf, R.R., 2003b, Using genetic algorithms in sub-pixel mapping. *International Journal of Remote Sensing*, **24**, pp. 4241–4247.

Nguyen, M.Q., Atkinson, P.M. and Lewis, H.G., 2005, Superresolution mapping using a Hopfield neural network with LIDAR data. *IEEE Geoscience and Remote Sensing Letters*, **2**, pp. 366–370.

Shen, Z., Qi, J. and Wang, K., 2009, Modification of pixel-swapping algorithm with initialization from a sub-pixel/pixel spatial attraction model. *Photogrammetric Engineering & Remote Sensing*, **75**, pp. 557–567.

Tatem, A.J., Lewis, H.G., Atkinson, P.M. and Nixon, M.S., 2001a, Super-resolution target identification from remotely sensed images using a Hopfield neural network. *IEEE Transactions on Geoscience and Remote Sensing*, **39**, pp. 781–796.

Tatem, A.J., Lewis, H.G., Atkinson, P.M. and Nixon, M.S., 2001b, Super-resolution mapping of urban scenes from IKONOS imagery using a Hopfield neural network. In *Proceedings of the International Geoscience and Remote Sensing Symposium* (Sydney: IEEE), pp. 3200–3202.

Tatem, A.J., Lewis, H.G., Atkinson, P.M. and Nixon, M.S., 2002, Super-resolution land cover pattern prediction using a Hopfield neural network. *Remote Sensing of Environment*, **79**, pp. 1–14.

Teerasit, K., Arora, M.K. and Varshney, P.K., 2005, Super-resolution land-cover mapping using a Markov random field based approach. *Remote Sensing of Environment*, **96**, pp. 302–314.

Thornton, M.W., Atkinson, P.M. and Holland, D.A., 2006, Sub-pixel mapping of rural land cover objects from fine spatial resolution satellite imagery using super-resolution pixel-swapping. *International Journal of Remote Sensing*, **27**, pp. 473–491.

Verhoeye, J. and De Wulf, R.R., 2002, Land-cover mapping at sub-pixel scales using linear optimization techniques. *Remote Sensing of Environment*, **79**, pp. 96–104.

Wang, L., Zhang, Y. and Li, J., 2006, BP neural network based sub-pixel mapping method. In *International Conference on Intelligent Computing*, pp. 755–760.

Yi, C., Pan, Y. and Zhang, J., 2006, Multiple-class land cover mapping at sub-pixel scale using an innovated CA model. In *Proceedings of the International Geoscience and Remote Sensing Symposium*, pp. 968–971.

Zhang, L., Wu, K., Zhong, Y. and Li, P., 2008, A new sub-pixel mapping algorithm based on a BP neural network with an observation model. *Neurocomputing*, **71**, pp. 2046–2054.

Zhi, X.H., Xing, X.L., Wang, Q.X., Zhang, L.H., Yang, X.W., Zhou, C.G. and Liang, Y.C., 2004, A discrete PSO method for generalized TSP problem. In *Proceedings of the 2004 International Conference on Machine Learning and Cybernetics*, pp. 2378–2383.